Monthly Notices of the ROYAL ASTRONOMICAL SOCIETY

MNRAS **498,** 5263–5272 (2020)
Advance Access publication 2020 September 10

doi:10.1093/mnras/staa2613

Average cometary ion flow pattern in the vicinity of comet 67P from moment data

Hans Nilsson [1]★ Hayley Williamson,[1] Sofia Bergman [1] Gabriella Stenberg Wieser [1]★ Martin Wieser,[1] Etienne Behar [1,2] Anders I. Eriksson [3] Fredrik L. Johansson [3] Ingo Richter[4] and Charlotte Goetz [5]

[1]*Swedish Institute of Space Physics, Box 812, SE-981 28 Kiruna, Sweden*
[2]*Laboratoire de Physique des Plasmas, CNRS – École Polytechnique – CNRS – Sorbonne Université – Unversité Paris Saclay – Observatoire de Paris-Meudon, F-91128 Palaiseau Cedex, France*
[3]*Swedish Institute of Space Physics, Box 537, 751 21 Uppsala, Sweden*
[4]*Institut für Geophysik und extraterrestrische Physik, Technische Universität Braunschweig, Mendelssohnstr 3, D-38106 Braunschweig, Germany*
[5]*ESTEC, European Space Agency, Keplerlaan 1, NL-2201AZ Noordwijk, the Netherlands*

Accepted 2020 August 21. Received 2020 August 10; in original form 2020 June 29

ABSTRACT

Average flow patterns of ions around comet 67P detected by the RPC-ICA instrument onboard *Rosetta* are presented both as a time series and as a spatial distribution of the average flow in the plane perpendicular to the comet – Sun direction (*Y*–*Z* plane in the coordinate systems used). Cometary ions in the energy range up to 60 eV flow radially away from the nucleus in the *Y*–*Z* plane, irrespective of the direction of the magnetic field, throughout the mission. These ions may however be strongly affected by the spacecraft potential, the uncertainty due to this is briefly discussed. Inside the solar wind ion cavity and in the periods just before and after, the cometary pick up ions moving antisunward are deflected against the inferred solar wind electric field direction. This is opposite to what is observed for lower levels of mass-loading. These pick up ions are behaving in a similar way to the solar wind ions and are deflected due to mass-loading. A spatial asymmetry can be seen in the observations of deflected pick up ions, with motion against the electric field primarily within a radius of 200 km of the nucleus and also in the negative electric field hemisphere. Cometary ions observed by RPC-ICA typically move in the antisunward direction throughout the mission. These are average patterns, full-resolution data show very much variability.

Key words: plasmas – methods: data analysis – comets: individual: 67P.

1 INTRODUCTION

Comets are Solar system bodies containing a significant amount of volatiles which are released into surrounding space when they are heated. For typical comets in highly elliptical orbits the outgassing of volatiles, the comet activity, increases strongly as the comet approaches the Sun. The resulting gas and dust envelope, the coma, is gravitationally unbound, expanding into space with a velocity of typically 500–1000 m s^{-1} (Gulkis et al. 2015). The coma is ionized by solar extreme ultraviolet, solar wind electron impact ionization, and charge exchange with the solar wind (Galand et al. 2016; Simon Wedlund et al. 2017).

The expanding plasma of the coma, the comet ionosphere, is immersed in the solar wind. The two plasmas fill some common volume where they affect each other, though dense and large enough comas may expel the solar wind from their innermost regions. In the common volume, the solar wind is affected by the added mass of the newly formed cometary ions, in a process known as mass-loading (Szegö et al. 2000). The effect on both plasmas is dependent on the size of the coma plasma cloud in terms of cometary ion gyro radii. A newborn cometary ion experiencing the effect of the solar wind electric and magnetic field will have a gyroradius of order 10^4 km at 1 au from the Sun. Such a newborn ion accelerated by the solar wind electric field is said to be 'picked up' by the solar wind and becomes a 'pick up' ion.

For comet ionospheres that are large compared to a pick up ion gyroradius, such as that of Halley during the *Giotto* encounter, the effect is a slow down of the solar wind and the eventual formation of a weak, mass-loaded shock (Biermann, Brosowski & Schmidt 1967; Ogino, Walker & Ashour-Abdalla 1988). The shock already forms at a pick up ion number density of 3–4 per cent of the solar wind density. At Halley, the bow shock was found at about 1000 000 km distance from the nucleus (Galeev et al. 1986; Neubauer et al. 1986). Closer to the nucleus a cometosheath is found, bounded by a magnetopause where cometary ions start to dominate (Gombosi 1987). Closer yet to the nucleus the solar wind origin magnetic field is excluded from the innermost, densest region of the coma and a diamagnetic cavity is formed (Neubauer et al. 1986; Cravens 1989).

When the comet plasma cloud is much smaller than a pick-up ion gyroradius, as was the case for much of the escort phase of *Rosetta* following comet 67P (Nilsson et al. 2017), the situation is different. The mass-loading of the solar wind results in a deflection of the solar wind with very little slowing down (Behar et al. 2016, 2017,

★ E-mail: hans.nilsson@irf.se (HN); gabriella@irf.se (GSW)

2018a). The deflection is in the direction opposite to the solar wind electric field, essentially conserving momentum corresponding to the acceleration of cometary ions along the same electric field. As comet 67P approached perihelion, the size of the magnetosphere grew and a solar wind ion cavity formed (Behar et al. 2017; Nilsson et al. 2017). Closer to the nucleus a diamagnetic cavity formed, just as for the larger comet ionospheres (Goetz et al. 2016a, b). When *Rosetta* was located inside the solar wind ion cavity a full scale bow shock may have formed further away from the nucleus. Some traces of this have been observed. An asymmetric smaller scale shock-like structure, an infant shock, was seen intermittently (Gunell et al. 2018). Cometary ion data observed inside the solar wind ion cavity can be interpreted as a remote detection of a shock (Nilsson et al. 2018), in agreement with hybrid simulations (Alho et al. 2019).

The general flow pattern of ions in a small-scale ionosphere, a plasma cloud, is governed by the local electric fields (Nilsson et al. 2018). These are the solar wind electric field (Behar et al. 2016), the polarization electric field arising from the different behaviour of unmagnetized ions (on these small subgyro-radius scales) and the magnetized electrons (Brenning et al. 1991; Halekas et al. 2016; Nilsson et al. 2018, Gunell et al. 2019), and the ambipolar electric field associated with hot electrons in the steep density gradient of the expanding comet ionosphere (Madanian et al. 2016; Odelstad et al. 2018). The effect of the different electric fields on the cometary ions was reported in Berčič et al. (2018) for two selected periods with relatively constant nucleus and heliocentric distances. For more energetic cometary ions, above about 60 eV, the flow in the plane orthogonal to the Sun direction was along the solar wind electric field. Lower energy cometary ions showed a radial expansion in this plane regardless of the direction of the solar wind electric field, implying a dominant ambipolar electric field. For both components the antisunward flow direction dominated, implying the importance of the polarization electric field (Nilsson et al. 2018).

In this study, we use the RPC-ICA moment data delivered to Planetary Science Archive (PSA) to extend the work of Berčič et al. (2018) to the entire *Rosetta* mission. We look at the average flow direction of cometary ions binned into different spatial regions in the Comet Sun Electric (CSE) field coordinate system Y–Z plane (with X towards the Sun and Z orthogonal to X and along the solar wind electric field). The study also serves as a summary of the ion moment data as a reference for future more detailed studies. The data have not been corrected for spacecraft potential effects (Bergman et al. 2020a), it describes the data ‘as measured’.

2 METHODS

2.1 Instrument description

The primary data for this study come from the RPC-ICA mass-resolving ion spectrometer (Nilsson et al. 2007). RPC-ICA has an energy range of a few eV to 40 keV and a near 2π *sr* field of view. The time for an energy scan is 12 s, and a full field of view is covered in 192 s. Updates of the energy tables since the instrument paper was published are discussed in Nilsson et al. (2015a, b) and Stenberg Wieser et al. (2017). The instrument has sufficient mass resolution to divide the data into H^+, He^{2+}, He^+, and heavier ions of cometary origin, assumed here to have the mass/charge 18, i.e. H_2O^+.

The *Rosetta* Langmuir probe RPC-LAP consists of two Langmuir probes mounted on booms (Eriksson et al. 2007). RPC-LAP can provide estimates of plasma density, electron temperature, spacecraft potential, and for suitable conditions the electric field. In this study, RPC-LAP data are used to obtain an estimate of the spacecraft potential (Odelstad et al. 2017).

Rosetta magnetic field data (Glassmeier et al. 2007; Goetz et al. 2016a) is used to obtain an estimate of the direction of the magnetic field, from which the direction of the undisturbed solar wind electric field is found (Behar et al. 2016). Due to magnetic pollution from the spacecraft, the magnetic field magnitude and direction is not always correct. We have chosen to use the data without any particular threshold on magnitude, but instead compare some results with an alternative approach to estimate the solar wind electric field direction from the solar wind deflection direction as discussed by Behar et al. (2017).

2.2 Data set used

We have used the publicly available *Rosetta* data from the PSA. At the time of submission not all data have been ingested. For RPC-ICA, we use the L5 moment data, which is based on the L4 PHYS MASS data set, which contains data separated into the same physical mass ranges used in this paper, i.e. H^+, He^{2+}, He^+, and H_2O^+. Note that the H_2O^+ mass range may contain heavier ions (mainly CO_2^+ and other ions resulting from chemical reactions). The moment calculations have been done assuming a mass per charge of 18. In the later part of the mission, with summer in the Southern hemisphere, this may be an underestimate, as there was significant CO_2^+ outgassing (Hansen et al. 2016; Hoang et al. 2019) which close to the nucleus would result in a higher mean ion mass of up to about 35 a.m.u. per charge (Nicalaou et al., in preparation). Thus the velocities close to the nucleus during the post-perihelion part of the mission may be overestimated with up to a factor 2.

The full moment data set consists of about 160 000 data points of 192 s length obtained over a period of about 2 yr, from 2014 August to end of 2016 September. RPC-ICA was regularly off during and just after wheel off-loadings, and sometimes operated in a two-dimensional low energy high time resolution mode (Stenberg Wieser et al. 2017) which is not included in the moment data set.

The moment data are a numerical integration over the available field of view. No fitting or extrapolation to uncovered viewing directions has been done. We define the moments and provide equations on how they are calculated from the data in Appendix A. The moment calculations are described in more detail in Behar (2018) and a general description of moment calculations for an almost identical instrument on Mars Express can be found in Fränz et al. (2006).

The cometary ion data have been divided into two energy ranges, above and below 60 eV. This is because the ions exhibit different behaviour above and below this approximate limit as shown in Berčič et al. (2018) and further discussed later in this study.

As discussed in Berčič et al. (2018), the incomplete field of view of the RPC-ICA instrument may affect the results. Most of the time *Rosetta* was in a nadir-pointing terminator orbit. For such orbits RPC-ICA has a free $180^\circ \times 90^\circ$ field of view centred on the nucleus. The field of view with a component towards the Sun is partly obscured. The field of view of RPC-ICA is illustrated in Nilsson et al. (2007, 2015a). The obstruction can give abrupt changes of the ion flux as it moves in and out of the field of view. For the average data, we present here we note that sunward and antisunward flow components for flow away from the nucleus have equal free field of view. For cometward flow, the spacecraft blocks about half of the field of view, and the solar panel blocks a bit more of flow which is simultaneously cometward and sunward.

An important note about the data set is that it has not been corrected for any possible effect due to the significantly negative

Figure 1. Panels (a)–(d) show the ion velocity [km s^{-1}] around comet 67P from 2014 August to 2016 September, in CSEq coordinates. Panel (a) shows H^+, (b) He^{2+}, (c) H_2O^+ for energy above 60 eV, and (d) H_2O^+ for energy below 60 eV. Panel (e) shows the position of *Rosetta* relative to the nucleus in CSEq coordinates. In all panels colours red, blue, and green corresponds to the *X*, *Y*, and *Z* components, respectively. The data are averaged over 24 h.

spacecraft potential. Work is ongoing to evaluate the effect on this data set (Bergman et al. 2020a, b). We will here only make a first discussion based on the already published work. The spacecraft potential was typically in a range from −10 to −30 V, meaning that ions with energy above 60 eV were typically not strongly affected by the spacecraft potential.

3 OBSERVATIONS

3.1 Low-resolution time series

The velocity of ions as observed by RPC-ICA during the period from 2014 August 1 to 2016 September 30 is shown in Fig. 1. The data are shown in the Comet–Sun–Equatorial (CSEq) coordinate system. The primary vector is X_{CSEq}, directed from the nucleus towards the Sun. Z_{CSEq} is the component of the Sun's north pole to date orthogonal to X_{CSEq}. Y_{CSEq} completes a right-handed system. To only show the large-scale features, the data have been averaged over 24 h, about two comet rotations. To give low statistical weight to low-density measurements, the flux calculated from the data set (density times velocity) has been summed over 24 h and then divided by the sum of the density of the same data set. The actual variability of the data is much larger than for this averaged data set, but that will be the subject of another study.

Fig. 1(a) shows the H^+ velocity, (b) the He^{2+} velocity, (c) the H_2O^+ velocity for ions with an energy above 60 eV, (d) the same for ions with energy below 60 eV, and (e) shows the position of *Rosetta* relative to the nucleus. In all cases red, blue, and green (dark, medium, and light in grey-scale) represents the *X*, *Y*, and *Z* components, respectively. The lack of H^+ and He^{2+} around perihelion is the solar wind ion cavity (Behar et al. 2017; Nilsson et al. 2017). The deflection of the solar wind is clearly seen in the X_{CSEq} component (red) of H^+ and He^{2+}, with the flow direction turning positive (sunward) in the time before and after the solar wind ion cavity, in agreement with previous studies. The cometary ions with energy more than 60 eV (pick up ions) have a dominating antisunward component, in agreement with previous studies (Nilsson et al. 2017). The low-energy (<60 eV) cometary ions have a significant antisunward component, but most prominent is a systematic variation of the Y_{CSEq} and Z_{CSEq} components. Closer inspection shows that the *Y* and *Z* components varies with the same period but a phase shift. A comparison with panel (e) shows that the velocity is correlated with the position of *Rosetta* relative to the nucleus. We show in Section 3.2 that this is due to a radial outflow of the low-energy cometary ions in the *Y*–*Z* plane, giving rise to the consistent behaviour of the *Y* and *Z* components of the velocity and position of the spacecraft.

In order to see the effect of the solar wind electric and magnetic field, the same data are shown in Fig. 2 in the CSE reference frame.

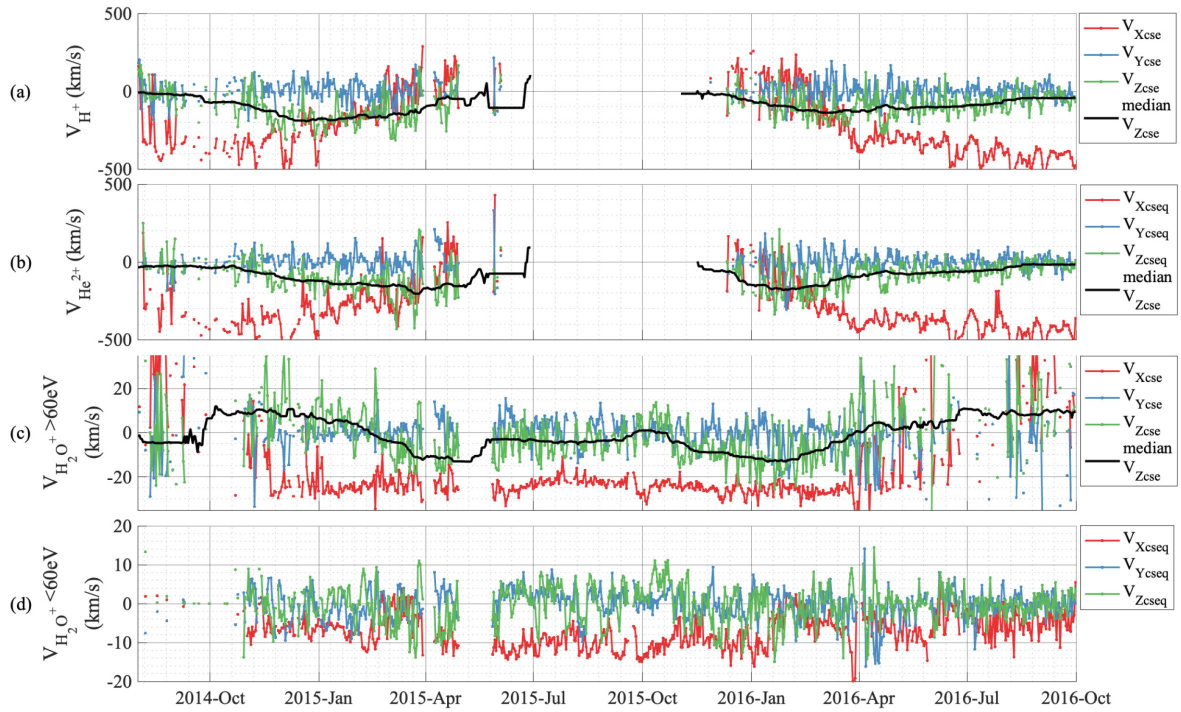

Figure 2. Panels (a)–(c) show the ion velocity [km s^{-1}] around comet 67P from 2014 August to 2016 September, in CSE coordinates. Panel (a) shows H^+, (b) He^{2+}, (c) cometary ions for energy above 60 eV, and panel (d) cometary ions for energy below 60 eV. In all panels colours red, blue, and green corresponds to the *X*, *Y*, and *Z* components, respectively. The data are averaged over 24 h. In panels (a)–(c), a black line indicates a 50 d running median value for the *Z* component, to show the trend of the sign of the signal more clearly.

X_{CSE} points towards the Sun, Z_{CSE} is orthogonal to X_{CSE} and along the solar wind electric field. Y_{CSE} completes a right-handed system. The solar wind electric field can be inferred from either the magnetic field direction or the direction of the proton deflection (Behar et al. 2017). We have used the magnetic field in this study, shown in other studies to be a very good proxy for most of the mission (Edberg et al. 2019). The electric field direction is then given from the assumption that the solar wind is $E \times B$ drifting in the *X*-direction, so that

$$\boldsymbol{E} = -\boldsymbol{v} \times \boldsymbol{B}. \tag{1}$$

It is the electric and magnetic field in the *Y*–*Z* plane that is important for the $E \times B$ drift in the *X* direction. Thus the simplified approach of rotating the coordinate system in the *Y*–*Z* plane to align with the upstream solar wind electric/magnetic field in this plane is mostly used for Solar system bodies. An example is the Mars–Solar wind–Electric field coordinate system (Barabash et al. 2007). This also has the advantage of keeping the *X*-direction the same. From equation (1) also follows that the magnetic field in the *Y*–*Z* plane is along *Y*. This is the approach used in this study. Taking a full three-dimensional view shows that there is also a consistent drift towards dawn for cometary ions and towards dusk for solar wind ions (Behar, Tabone & Nilsson 2018b).

Fig. 2(a) shows the H^+ velocity. The difference from the CSEq frame is that now the *Z* component is quite consistently negative. To emphasize this trend, we show the *Z* component filtered using a 50 d running median using a thick black line in Fig. 2. This is not true for very low activity (large heliocentric distances) and for the period just before and after the solar wind ion cavity. The negative *Z* component corresponds to a motion of the solar wind in the opposite direction to the inferred solar wind electric field. The momentum of the deflected solar wind ions balances the momentum of pick up ions accelerated in the opposite direction along the electric field. It can also be seen as the solar wind ions gyrating in the mass-loaded plasma (Behar et al. 2018a).

In the regions where the H^+ is clearly deflected in the negative *Z* direction, the cometary ions with energy above 60 eV (Fig. 2b) have a positive *Z* component, as expected if they are accelerated by the solar wind electric field. In the regions of sunward H^+ flow and in the solar wind ion cavity, these ions have a negative *Z* component. To check for the possibility that this is because of problems with the magnetic field data, we have also oriented this data according to the H^+ flow direction in the *Y*–*Z* plane, i.e. assuming *E* is along the H^+ flow direction (not shown). This does not provide data in the solar wind ion cavity, but outside it provides a consistent pattern regarding the pick up ion flow. It is still towards negative Z_{CSE} in the region of sunward solar wind flow just outside the solar wind ion cavity, and otherwise towards positive Z_{CSE}.

The regular pattern in the low energy ion (<60 eV) velocity *Y* and *Z* components is now gone. This can be expected, as the position of *Rosetta* in the CSE reference frame does not vary slowly in a consistent manner, the way it did for the CSEq coordinate system.

Finally, we note that there is sunward flow in the pick up ions very early and late in the mission. This is mostly a signal from sectors 0 and 15 which at times are noisy. Some of this signal may be real, most of it is believed to be noise or cross-talk. We leave it out of the discussion in this study.

3.2 Flow in the *Y*–*Z* plane

In order to study the radial expansion further, the average flow in different spatial bins in the *Y*–*Z* plane is shown in Fig. 3, for both CSEq (upper left panel) and CSE frames. Note that these plots show

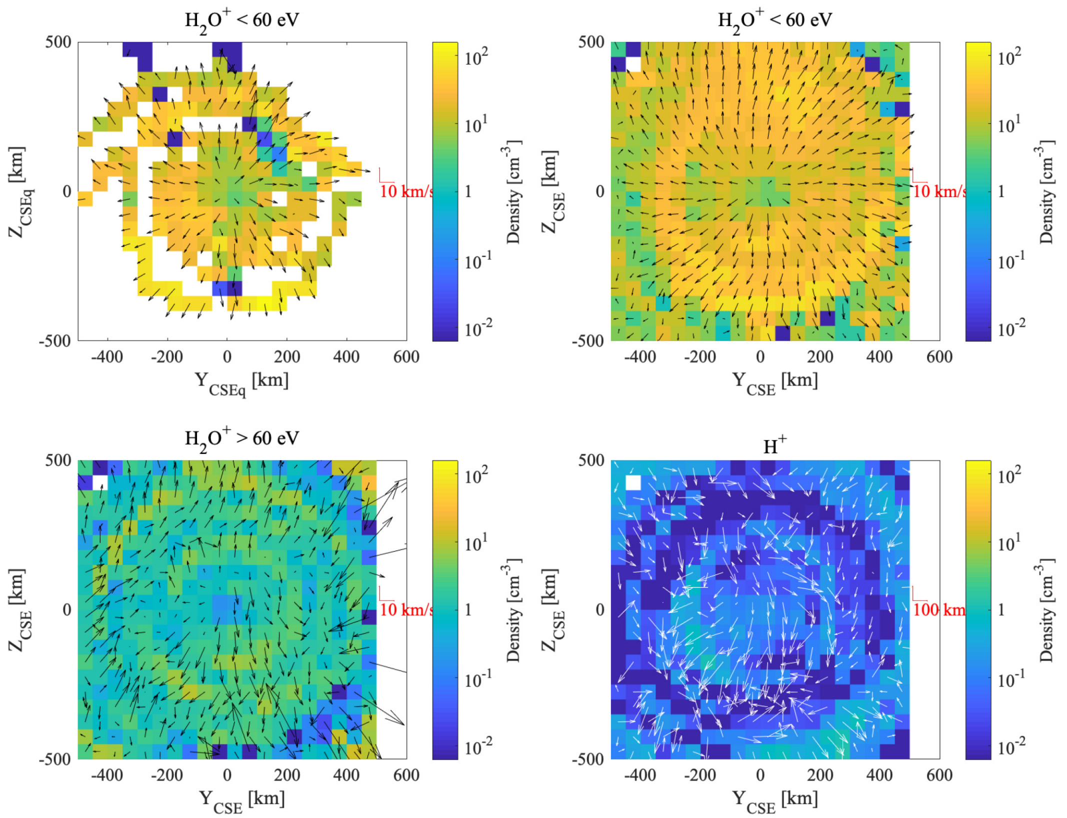

Figure 3. Average flow pattern in the *Y–Z* plane for the entire escort phase (2014 August to 2016 September) shown as arrows, with the corresponding average density for four different ion populations (cm^{-3}). The velocity scale is given by red arrows in the middle right part of the panels (km s^{-1}). The upper left panel shows cometary ions with energy less than 60 eV in CSEq coordinates, while the upper right panel shows the same in CSE coordinates. The lower left panel shows cometary ions with energy more than 60 eV in CSE coordinates and the lower left H^+ in CSE coordinates.

spatial averages of all data, with biased sampling in the sense that larger distances were typically sampled for higher cometary activity and during the excursions. The plots are mainly intended to show the consistency of the regular flow pattern seen in the low-energy cometary ions in Fig. 1 and what the corresponding flow looks like for solar wind ions, pick up ions and in the CSE coordinate system. All panels show the average velocity in the *Y–Z* plane with an arrow, with the length corresponding to the magnitude of the velocity. A length-scale is given by two red arrows in the panel. The colour scale gives the average ion density in the spatial bin. The bins are projections such that the *X* component is not taken into account. Much of the *Rosetta* data were taken in the terminator plane, see Fig. 1(e), but much of the data for a radius in the *Y–Z* plane larger than 300 km is dominated by the dayside excursion. Doing the same plot for a smaller range of distances and higher resolution (down to 100 at 10 km resolution) shows a consistent pattern of radial expansion in the *Y–Z* plane (not shown). The upper left panel shows the low-energy cometary ions in the CSEq coordinate system, while the upper right panel shows the same in the CSE system. The lower left panel shows the pick up ions with an energy above 60 eV, while the lower right panel shows H^+, both in CSE coordinates.

Both the upper panels show a clear radial expansion, with rather constant average speed in the *Y–Z* plane regardless of the distance to the nucleus. The innermost part does show lower velocities, and this should be investigated further in another study concentrating on that region. There does not appear to be any strong asymmetry whether the ions are moving along or across the magnetic field (CSE coordinates, upper right panel, along B is in $\pm Y$ direction, across in

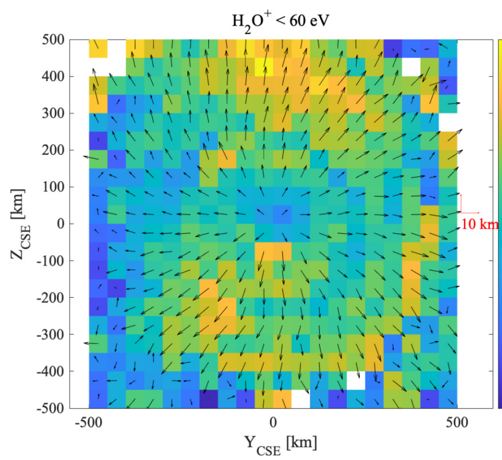

Figure 4. Average flow pattern in the *Y–Z* plane (CSE coordinates) for the entire escort phase (2014 August to 2016 September) shown as arrows, for cometary ions with energy below 60 eV. The velocity scale is given by red arrows in the middle right part of the panels (km s^{-1}). The colour scale gives the magnitude of the velocity in the *Y–Z* plane.

the $\pm Z$ direction). To investigate any degree of acceleration further, we show in Fig. 4 the same ion flow as in Fig. 3 upper right panel, but with the magnitude of the velocity in the *Y–Z* plane colour coded.

Fig. 4 shows that there is a consistent increase of the velocity towards positive *Z*, i.e. along the solar wind electric field direction.

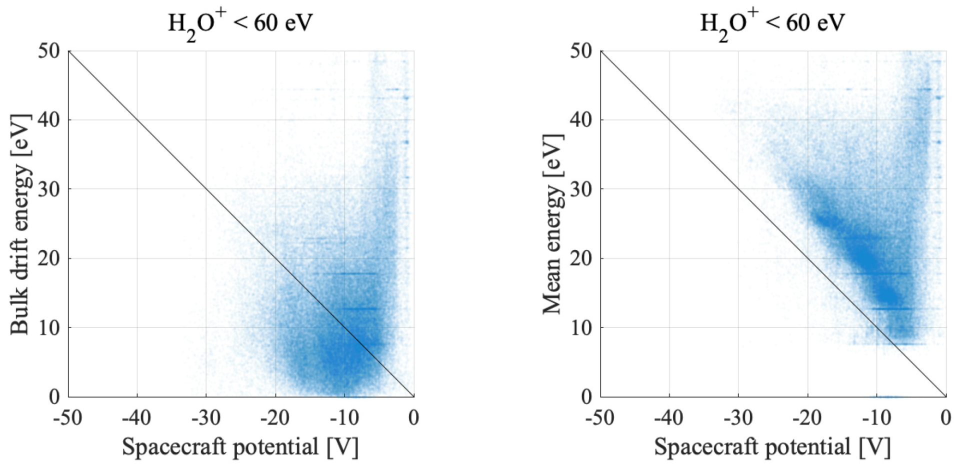

Figure 5. The bulk drift energy (left) and the mean particle energy (right) in eV as function of the spacecraft potential (V). The bulk drift energy is calculated using the magnitude of the velocity moment. The mean particle energy is calculated by adding energy spectra from all different directions for each full directional measurement cycle and then calculating mean particle energy.

One must however note that these figures are showing data from the whole mission, and typically data at larger distances were obtained for higher activity. The usefulness is rather to illustrate the consistency of the low-energy cometary ion flow in the *Y*–*Z* plane throughout the mission.

The pick up ions show a more complicated pattern. For negative *Z* in the centre, for a radius less than about 300 km, and for positive *Y*, they are mostly moving towards negative *Z*, against the electric field. At negative *Y* and positive *Z* they are mostly moving towards positive *Z*.

The H^+ is mainly moving towards negative *Z* and away from the nucleus within a distance of about 300 km. In addition to that the flow in the *Y*-direction is quite consistent over different parts of the *Y*–*Z* plane, i.e. towards negative *Y* upper right corner and towards positive *Y* in the upper left and lower right corner.

3.3 The influence of the spacecraft potential

The spacecraft potential can have a very strong influence on the trajectory of low-energy ions. *Rosetta* most of the time had a negative spacecraft potential (Odelstad et al. 2017), thus accelerating positive ions towards the spacecraft. The effect of the spacecraft potential has been studied for the *Rosetta* spacecraft (Bergman et al. 2020a, b), ions at an energy corresponding to less than twice the spacecraft potential may have severely distorted trajectories. We note that in the study of Bergman et al. (2020a), it was found that certain sectors and elevations were less affected than other. A general trend was that one pixel was good, and surrounding pixels showed a distortion away from this central location, thus exaggerating the angular distance from this centre. In particular sector 5 and elevation 10 was such a centre (see Nilsson et al. (2007) for definition of sectors and elevation indices). Sector 5 is around where most of the cometary ions are observed (Nilsson et al. 2015b), with an elevation typically between 8 and 11. To fully understand the effect of the spacecraft potential requires making use of the simulations performed by Bergman et al. (2020a), which is beyond the scope of this study.

The moments used here are calculated as measured by the instrument with no attempt to compensate for the spacecraft potential. This is thus representative also of the results obtained using any lower level RPC-ICA data. ICA low-energy data also suffers from less elevation angle coverage, see the RPC-ICA User Guide on the PSA archive. For energies below 20 eV coverage is very poor (1–3 elevation bins) while above 50 eV the elevation range is close to nominal but coarse, and above 100 eV it is nominal.

In order to get a first assessment of the possible impact of the spacecraft potential on our data, we estimate the effect empirically. Fig. 5 shows how the bulk drift energy (left-hand panel) and the mean particle energy (right-hand panel) for ions with energy less than 60 eV depend on the spacecraft potential as determined from the RPC-LAP instrument. The spacecraft potential is shown on the *x*-axis. Bulk drift energy is the kinetic energy corresponding to the velocity moment used in this study. The particle mean energy is calculated by summing the energy spectra of the distribution function over all directions, then calculating the mean energy of this 1D distribution, as was done in Behar et al. (2017). This value thus corresponds to the energy of the particles regardless of their direction. As can be seen the bulk drift energy has no dependence on the spacecraft potential. The particle mean energy is shifted up with the spacecraft potential, and is 5–10 eV higher than the spacecraft potential. This is not enough to avoid influence on the trajectories of the ions. The lack of correlation between the bulk drift energy and the spacecraft potential indicates that our consistent results are not caused by a very low energy population being accelerated by the spacecraft potential along a trajectory determined solely by the spacecraft potential. We also calculated the moments using data only from the energy range 30–60 eV with virtually indistinguishable results from the ones shown in this study (not shown). As a further test we did the same, but only for a spacecraft potential above (less negative than) −10 V. This severely affected the time series plot, having much less data, but the *Y*–*Z* plot showed the same features as before (not shown).

We therefore show the data ‘as is’ here, and this is what has been delivered to the PSA (Besse et al. 2018). Once we understand the effect of the spacecraft potential better we may need to revise these results. We currently believe that this will not much affect the results we report here, but that there may be yet another population at the lowest energies, more locally produced and less accelerated, which we can hopefully study using RPC-ICA once we better understand the effect of the spacecraft potential.

4 DISCUSSION

The moment data used in this study reproduce features already reported in other studies using the full information of the data set. The

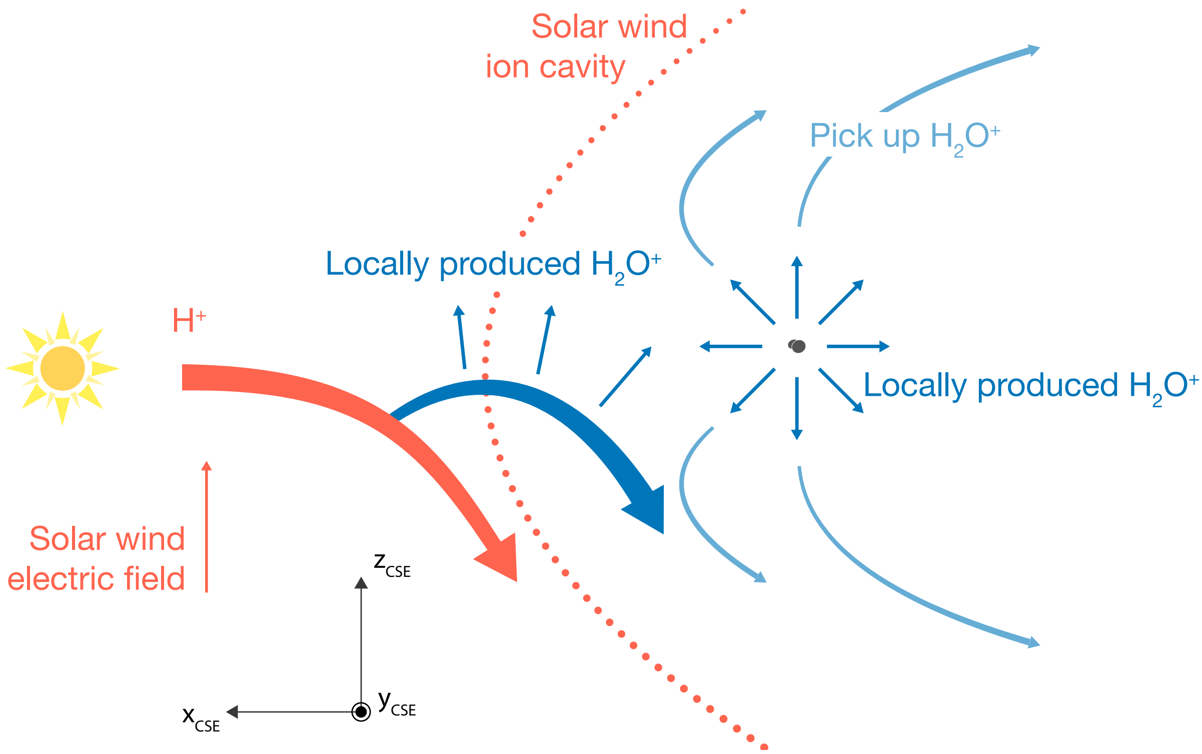

Figure 6. Schematic of ion flows observed around comet 67P in the X_{CSE}–Z_{CSE} plane. A borad red arrow shows the solar iwnd ions, a broad blue arrow cometary pick up ions (>60 eV) and shorter thinner blue arrows show the flow direction of locally produced water ions. The thinnest blue lines show the inferred flow paths of initially radially expanding ions which at observation have an antisunward component to their flow direction.

solar wind is gradually more deflected with increased comet activity. The bulk velocity of the solar wind turns sunward at high enough activity, and for even higher activity *Rosetta* was inside a solar wind ion cavity (Behar et al. 2017). The pick up ions (more than 60 eV cometary ions) flow mainly antisunward (Nilsson et al. 2015b, 2017). The low-energy cometary ions move radially away from the nucleus in the *Y*–*Z* plane (Nilsson et al. 2015b, 2017; Berčič et al. 2018), with a significant, often dominating antisunward component. A schematic of this flow is shown with thin blue arrows in the right hand part of Fig. 6.

The average flow direction is from the direction where RPC-ICA has the largest unobstructed field of view. This could thus be an artefact of the instrument field of view. The data were frequently seen in a relatively narrow angular range well within the field of view (Nilsson et al. 2015b), showing that this general feature is not an artefact of the instrument. For flow from the nucleus, the sunward and antisunward flow directions are equally sampled. As part of the ESA enhanced archive effort we also attempted to create a flag indicating when the maximum signal was at the edge of the instrument field of view. The predictive power for the solar wind density estimate was low and the flag was not used. It did however show that for 92 per cent of the cases the peak of the cometary ion signal was not at the edge of the field of view. An incomplete field of view as that of RPC-ICA will always cause uncertainties that cannot be fully resolved. The results we present here forms a coherent picture of what occurred within the RPC-ICA field of view. The clear maximum signal within the field of view indicates that if something is missing, it is an additional population quite consistently outside the RPC-ICA field of view.

The moment data transformed into the CSE coordinate system confirms and extends some previous findings. The radial expansion of low-energy ions in the *Y*–*Z* plane is almost independent of the direction of the solar wind electric and magnetic field as shown for shorter time periods by Berčič et al. (2018). Here, we see that it is a general feature observed throughout the mission. The flow speed component in the *Y*–*Z* plane of the ions observed by RPC-ICA has a median of 7 $\mathrm{km\,s^{-1}}$, much above the parent neutral gas. The median speed of the full vector including the *X* component is 11 $\mathrm{km\,s^{-1}}$. The radial flow component in the *Y*–*Z* plane does not change much with distance, indicating that most of the acceleration in the radial direction took place relatively close to the nucleus. Some effect where higher velocities at large distances are seen for positive Z_{CSE}, i.e. where we would expect the solar wind electric field and ambipolar diffusion to work in the same direction.

The weak effect of the direction of the magnetic field is particularly notable considering that such high velocities compared to the parent neutral gas have been attained also across the magnetic field. Ambipolar diffusion is the expected driver of the radial acceleration of cometary ions, but it is not expected to work across the magnetic field lines though this should depend on the electron gyroradius. At the position of *Rosetta*, the momentum flux of the low-energy cometary ions is not significant compared to pick up ions, solar wind and the magnetic field most of the time, while the electron pressure is often the most important pressure term (Williamson et al. 2020). Thus the expanding plasma may deform the magnetic field rather than being guided by it. This is clearly happening close enough to the nucleus, at the diamagnetic cavity boundary.

The density estimate of the low-energy population as seen by RPC-ICA is typically one or two orders of magnitude below the estimate from RPC-LAP or RPC-MIP (Trotignon et al. 2007; Hajra et al. 2017). The reason for this is not fully clear, but it likely means that the ions reported here are not representative of all low-energy plasma. The mean effective speed (bulk and thermal velcoity) of the ions in and around the diamagnetic cavity has been estimated to typically 2–4 $\mathrm{km\,s^{-1}}$ (Odelstad et al. 2018), with velocities up to about 10 $\mathrm{km\,s^{-1}}$ seen outside the cavity, in agreement with a mean effective speed in the range 2–8 $\mathrm{km\,s^{-1}}$ also reported by Vigren et al. (2017). The plasma observed by RPC-ICA typically have a higher velocity and may thus be a subset excluding the very lowest energy ions. To study these very lowest energy ions using RPC-ICA, we need to better understand the effect of the spacecraft potential.

The average solar wind flow in the CSE Y–Z plane is in the Z-direction, against the solar wind electric field as expected. The flow is more straight towards Z in the centre (about 200 km radius), just as for pickup ions. Otherwise there is no clear correlation between the flow patterns of pick up ions and solar wind ions in the Y–Z plane. The few cases of H^+ flow in the positive Z_{CSE} direction may indicate a problem with the reliability of the magnetic field data. However, all RPC-ICA data at higher time resolution do show significant scatter, including solar wind flow towards positive Z_{CSE} when the latter is determined from magnetic field data. The magnetic field data have uncertainties, in particular for low values of the magnetic field (Goetz et al. 2016a), so unreliability is more pronounced in the early and late parts of the mission. A few cases of sunward flow in the early data are most likely due to the real signal hitting a dead sector, and cross-talk being picked up by another sector. This seems to be a problem only for some early data.

The pick up ions are affected by the direction of the solar wind electric field as reported by Nilsson et al. (2015a), Behar et al. (2016), Berčič et al. (2018), and many others, which showed the pick up ions moving along the electric field. However, this turns out to be true only for low enough activity. For high enough activity, the pick up ions in the energy range above 60 eV are deflected in the direction against the solar wind electric field, just like the solar wind. We illustrate the situation in Fig. 6, where a red arrow indicates the deflected solar wind, and a similar blue arrow shows the initially accelerated and later deflected pick up ions.

This has been reported for cases of pick up ions inside the diamagnetic cavity (Masunaga et al. 2019) but can here be shown to be a general feature for the solar wind ion cavity and the period just before and after, with sunward solar wind flow. These pick up ions were created upstream and accelerated antisunward by the polarization electric field (Nilsson et al. 2015b, 2017, 2018; Behar et al. 2016). As these pick up ions enter a region of stronger mass-loading, they become deflected just like the solar wind ions. The pick up ions carry momentum into the solar wind ion cavity, having in practice taken over the role of the solar wind ions in this respect. Deflection against the solar wind electric field direction can be seen as the effect of conservation of momentum, but the physical mechanism is expected to be a gyration due to the magnetic field (Behar et al. 2018a). Nicolaou et al. (2017) showed in a case study how energy–angle dispersion of cometary ions indicates that the gyroradius of the cometary ions in the *Rosetta* vicinity is at least at times small enough that gyration starts to play a role. We finally note that the pick up ions carrying the momentum into the solar wind ion cavity, a region still dominated by the solar wind electric field, has similarities to the situation in the magnetic pile up boundary (MPB) at Mars. The MPB at Mars is a region where the solar wind magnetic field is piled up, while the protons are replaced by the locally produced ions (Sauer, Dubinin & Baumgärtel 1997; Dubinin et al. 2008). Bi-ion fluid models predict a similar behaviour for comets (Sauer, Bogdanov & Baumgärtel 1994).

The gyroradius of a new born ion is a function of the local electric and magnetic fields, the magnitude of the electric field in the mass-loaded solar wind is not directly measured. It can be obtained from simple models of the polarization electric field (Nilsson et al. 2018), semi-analytical models (Behar et al. 2018a) and full simulations (Koenders et al. 2016). The analytical model of Nilsson et al. (2018) estimates the electric field inside the solar wind ion cavity to be in the range 0.1–0.5 $\mathrm{mV\,m^{-1}}$ while the magnetic field was about 20 nT, although both very variable (Goetz et al. 2017). This would correspond to a gyroradius for a new born water ion of 50 km, clearly indicating that gyration can play a role around perihelion and that the bulk of ions born inside the coma, mostly shielded from the solar wind, may be $E \times B$ drifting on the scale of the coma. The pick up ions on the other hand have at least 60 eV energy by our definition, and up to typically about 1 keV. This yields a gyroradius of 200–1000 km for a 20 nT magnetic field. This indicates that gyration should play a role for the pick up ions, which have room to perform a part of a gyration within the coma, consistent with deflection.

Fig. 3 showed a particular spatial pattern of the pick up ion flow, with motion towards negative Z in the centre and for negative Z_{CSE}. Whereas one should be careful in reading too much into these simple spatial maps, in one sense this is not a temporal phenomena; it remains when the data are divided into inside/outside solar wind ion cavity (not shown). From the conservation of momentum/mass-loading perspective pick up ions must have passed through a comparatively dense part of the coma before observation in order to be moving against the solar wind electric field at the observation point. This is approximately consistent with the distribution of observed flow directions. One may note that there is another similar asymmetry in the coma reported, related to cold electrons. Edberg et al. (2019) reported that the presence of cold (<1 eV) electrons was more common in the Z_{CSE} hemisphere. These are electrons that have been cooled by collisions, presumably in a denser part of the coma, and then transported to the observation point. The transport of these electrons is apparently not inhibited across the magnetic field, and does follow the pick up ions.

The *Rosetta* spacecraft potential was often significantly negative. Positive ions are accelerated towards the spacecraft. Ions with an energy (prior to acceleration by the spacecraft potential) less than about twice the energy gained from the spacecraft potential can have their trajectories significantly distorted (Bergman et al. 2020a). What we can clearly say from the data we presented is that the bulk drift speed estimate is not a function of the spacecraft potential (Fig. 5 lower left panel). Ions in a range where the spacecraft potential should be less important (30–60 eV) also shows a radial expansion, as did the cometary ions during the nightside excursion, where ions reached much higher energy as *Rosetta* went far away from the nucleus, out to about 1000-km distance (Behar et al. 2018c). During the nightside excursion, the cometary ion flow was essentially radially away from the nucleus in all dimensions, not just the Y–Z plane, so it is not necessarily fully representative of cometary ion flow in the dayside. Flow continuity indicates that a radial flow must have occurred also closer to the nucleus. We therefore believe that, despite the fact that the trajectories of the lowest energy ions are severely distorted by the negative spacecraft potential, the radial expansion reported here is real.

5 CONCLUSIONS

The RPC-ICA moment data base which we have used reproduces the main features of many previous observations, notably the deflection of the solar wind, acceleration of pick-up ions along the solar wind electric field for the low-activity case, dominating antisunward flow of pick up ions and a radial expansion of low-energy cometary ions in the *Y–Z* plane (*X* towards the Sun).

We also find a number of new features. The radial expansion of the low-energy ions in the *Y–Z* plane is seen throughout the mission at all positions. The expansion is apparently not strongly affected by the electric and magnetic fields of the solar wind. A somewhat more sustained gradual acceleration out to large distances can be seen along the solar wind electric field direction (positive *Z* in CSE coordinates). We note that this result may be affected by the significantly negative spacecraft potential. Our current conclusion is that this radial expansion is not an artefact of the spacecraft potential as such, but future more accurate estimates taking the spacecraft potential into account may refine the picture. One should also note that the density of the population observed by RPC-ICA is much lower (1–2 orders of magnitude typically) than what is observed by RPC-LAP and RPC-MIP. This could mean that RPC-ICA detects a population of accelerated ions at an energy higher than more locally produced ions, or it could be an effect of the spacecraft potential, where the disturbed trajectories of a majority of ions prevent them from reaching RPC-ICA. The data have been delivered as is to the PSA, with no attempt to correct for the spacecraft potential. The spacecraft potential estimated from RPC-LAP is delivered with the RPC-ICA L4 data, interpolated to the times of RPC-ICA measurements.

Pick up ions in the solar wind ion cavity and in the surrounding regions of mainly sunward solar wind ion flow are deflected against the direction of the solar wind electric field. These ions are moving antisunward into a denser cometary plasma and are mass-loaded. Inside the solar wind ion cavity these pick up ions take on the role of the solar wind ions in the momentum transfer to the local ions. This has similarities to the magnetic pile up region at Mars where planetary ions replace the solar wind ions in a region dominated by the solar wind magnetic field (Dubinin et al. 2008). The mass-loaded pick up ions are mainly seen near the nucleus and in the negative electric field hemisphere.

ACKNOWLEDGEMENTS

Funding support comes from Swedish Research Council contract 2015-04187. We acknowledge use of the Planetary Science Archive (PSA, http://archives.esac.esa.int/psa)) for Rosetta MAG, LAP, MIP, and ICA data. We also acknowledge the use of AMDA (amda.cdpp.eu) for LAP and MIP data. C. Goetz is supported by an ESA Research Fellowship.

DATA AVAILABILITY

The data underlying this article have been submitted to the PSA and will be available through https://psa.esa.int. At the time of publication the RPC-ICA moment data are not yet ingested into the PSA data base. The data have been delivered and been through a first review. We are currently awaiting the outcome of a delta review of the data set needed before ingestion.

REFERENCES

Alho M., Simon Wedlund C., Nilsson H., Kallio E., Jarvinen R., Pulkkinen T., 2019, A&A, 630, A45
Barabash S., Fedorov A., Lundin R., Sauvaud J.-A., 2007, Science, 315, 501
Behar E., 2018, PhD thesis. Luleå Univ. Technology
Behar E., Nilsson H., Wieser G. S., Nemeth Z., Broiles T. W., Richter I., 2016, Geophys. Res. Lett., 43, 1411
Behar E., Nilsson H., Alho M., Goetz C., Tsurutani B., 2017, MNRAS, 469, S396
Behar E., Tabone B., Saillenfest M., Deca J., Holmström M., Nilsson H., 2018a, A&A, 620, A35
Behar E., Tabone B., Nilsson H., 2018b, MNRAS, 478, 1570
Behar E. et al., 2018c, A&A, 616, A21
Bergman S., Stenberg Wieser G., Wieser M., Johansson F. L., Eriksson A., 2020a, J. Geophys. Res., 125, e2019JA027478
Bergman S., Stenberg Wieser G., Wieser M., Johansson F. L., Eriksson A., 2020b, J. Geophys. Res., 125, e2020JA027870
Berčič L., Behar E., Nilsson H., Nicolaou G., Stenberg Wieser G., Wieser M., Goetz C., 2018, A&A, 613, A57
Besse S. et al., 2018, Planetary and Space Science, 150, 131
Biermann L., Brosowski B., Schmidt H. U., 1967, Sol. Phys., 1, 254
Brenning N., Kelley M. C., Providakes J., Stenbaek-Nielsen H. C., Swenson C., 1991, J. Geophys. Res., 96, 9735
Cravens T. E., 1989, J. Geophys. Res., 94, 15025
Dubinin E. et al., 2008, J. Geophys. Res., 113, A10217
Edberg N. J. T., Eriksson A. I., Vigren E., Johansson F. L., Goetz C., Nilsson H., Gilet N., Henri P., 2019, AJ, 158, 71
Eriksson A. I. et al., 2007, Space . Sci. Rev., 128, 729
Fränz M. et al., 2006, Space Sci. Rev., 126, 165
Galand M. et al., 2016, MNRAS, 462, S331
Galeev A. et al., 1986, Geophys. Res. Lett., 13, 841
Glassmeier K.-H., Boehnhardt H., Koschny D., Kührt E., Richter I., 2007, Space Sci. Rev., 128, 1
Goetz C. et al., 2016a, MNRAS, 462, S459
Goetz C. et al., 2016b, A&A, 588, A24
Goetz C., Volwerk M., Richter I., Glassmeier K.-H., 2017, MNRAS, 469, S268
Gombosi T. I., 1987, Geophys. Res. Lett., 14, 1174
Gulkis S. et al., 2015, Science, 347
Gunell H. et al., 2018, A&A, 619, L2
Gunell H., Lindkvist J., Goetz C., Nilsson H., Hamrin M., 2019, A&A, 631, A174
Hajra R. et al., 2017, MNRAS, 469, S372
Halekas J. S. et al., 2016, Geophys. Res. Lett., 43, 1426
Hansen K. C. et al., 2016, MNRAS, 462, S491
Hoang M. et al., 2019, A&A, 630, A33
Koenders C., Goetz C., Richter I., Motschmann U., Glassmeier K.-H., 2016, MNRAS, 462, S235
Madanian H. et al., 2016, J. Geophys. Res., 121, 5815
Masunaga K., Nilsson H., Behar E., Stenberg Wieser G., Wieser M., Goetz C., 2019, A&A, 630, A43
Neubauer F. M. et al., 1986, Nature, 321, 352
Nicolaou G., Behar E., Nilsson H., Wieser M., Yamauchi M., Bercic L., Stenberg Wieser G., 2017, MNRAS, 469, S339
Nilsson H. et al., 2007, Space Sci. Rev., 128, 671
Nilsson H. et al., 2015a, Science, 347, aaa0571
Nilsson H. et al., 2015b, A&A, 583, A20
Nilsson H. et al., 2017, MNRAS, 469, S252
Nilsson H. et al., 2018, A&A, 616, A50
Odelstad E., Stenberg-Wieser G., Wieser M., Eriksson A. I., Nilsson H., Johansson F. L., 2017, MNRAS, 469, S568
Odelstad E. et al., 2018, J. Geophys. Res., 123, 5870
Ogino T., Walker R. J., Ashour-Abdalla M., 1988, J. Geophys. Res., 93, 9568
Sauer K., Bogdanov A., Baumgärtel K., 1994, Geophys. Res. Lett., 21, 2255
Sauer K., Dubinin E., Baumgärtel K., 1997, Adv. Space Res., 20, 137
Simon Wedlund C. et al., 2017, A&A, 604, A73
Stenberg Wieser G., Wieser M., Yamauchi M., Nicolaou G., Behar E., Nilsson H., Berčič L., 2017, MNRAS, 469, S339
Szegö K. et al., 2000, Space Sci. Rev., 94, 429
Trotignon J. G. et al., 2007, Space Sci. Rev., 128, 713
Vigren E. et al., 2017, MNRAS, 469, S142
Williamson H., Nilsson H., Stenberg Wieser G., Eriksson A. I., Richter I., Goetz C., 2020, Geophys. Res. Lett., 47, e2020GL088666

APPENDIX A: MOMENT CALCULATIONS

The moment data presented in this work and delivered to the PSA is based on integration of the observed data. Missing data due to the limited field of view is then treated as if it was zero. The presentation is adopted from chapter 2 of Behar (2018), where more details can be found.

The basic definition of a moment of order k for a particle phase-space distribution function *f* is

$$\boldsymbol{M}^k = \int_v \boldsymbol{v}^k \times f(\boldsymbol{v})\, \mathrm{d}^3\boldsymbol{v}\ , \tag{A1}$$

where $\vec{v}$ is the velocity vector. For $k = 0$, we get the plasma particle density, or number density

$$n(\boldsymbol{r}) = \int_v f(\boldsymbol{v})\, \mathrm{d}^3\boldsymbol{v}\ . \tag{A2}$$

The data obtained from the instrument is in an instrument coordinate system where *f* is a function of energy and two angles that are usually referred to as the azimuth angle φ and the elevation angle θ. Note that θ is the angle out of the symmetry plane of the instrument, it is not a classical spherical coordinate system. Transformation from a Cartesian coordinate system to the instrument coordinate system is given by

$$n(\boldsymbol{r}) = \int_{-\infty}^{\infty}\int_{-\infty}^{\infty}\int_{-\infty}^{\infty} f(v_x, v_y, v_z) \quad \mathrm{d}v_x\, \mathrm{d}v_y\, \mathrm{d}v_z \tag{A3}$$

$$= \int_E \int_\varphi \int_\theta f(\boldsymbol{r}, E, \varphi, \theta)\sqrt{\frac{2E}{\mathrm{m}^3}}\cos(\theta) \quad \mathrm{d}E\mathrm{d}\varphi\mathrm{d}\theta. \tag{A4}$$

The data are obtained in discrete energy – angle bins, so that the numerical integration is in practice performed through sums given below for the zeroth-order (density) and first-order (velocity) moments. In these equations, c is the number of counts registered by the instrument in time τ for energy level E, with an instrument geometric factor of G, for a particle of mass m and Q elementary charges per particle. The energy is given in eV, which is why the elementary charge e is included in the equation. The instrument geometric factor is provided with the data in PSA, and in the units of $\mathrm{cm^{-2}\, sr^{-1}\, s^{-1}\, eV/eV}$. The factor 10^4 is for conversion to SI units. The angular width of one sector is $2\pi/16$, whereas the elevation angle is integrated over the angle $\Delta\theta(E)$ which is calculated from the elevation angle tables provided with the data delivered to PSA. Integration over energy is done with the variable ΔE which is calculated from the spacing of the energy table. Usually the energy table is marginally spare, meaning that gaps between energy steps are interpolated.

$$n(\vec{r}) = \frac{2\pi\ 10^4}{16\ \tau}\sqrt{\frac{m}{2e\ Q}} \cdot \sum_E \sum_\varphi \sum_\theta \times \left(\frac{1}{\sqrt{E^3}}\frac{\cos(\theta)}{G(E)} c(\vec{r}, E, \varphi, \theta) \quad \Delta E(E)\Delta\theta(E, \theta)\right) \quad [\mathrm{m^{-3}}] \tag{A5}$$

$k = 1$ corresponds to the flux density, with $\underline{\vec{u}}$ the flow velocity, or bulk velocity.

$$n(\boldsymbol{r})\, \underline{\boldsymbol{u}}(\boldsymbol{r}) = \int_v \boldsymbol{v}(\boldsymbol{r}) f(\boldsymbol{v})\, \mathrm{d}^3\boldsymbol{v} \tag{A6}$$

$$\underline{u_x}(\boldsymbol{r}) = \frac{2\pi\ 10^4}{16\, n(\boldsymbol{r})\, \tau}\sum_E \sum_\varphi \sum_\theta \frac{\cos 2(\theta)\cos(\varphi)}{E}\frac{c(\boldsymbol{r}, E, \varphi, \theta)}{G(E, \varphi, \theta)} \Delta E(E)\Delta\theta(E, \theta) \quad [\mathrm{m\, s^{-1}}] \tag{A7}$$

$$\underline{u_y}(\boldsymbol{r}) = \frac{2\pi\ 10^4}{16\, n(\boldsymbol{r})\, \tau}\sum_E \sum_\varphi \sum_\theta \frac{\cos 2(\theta) sin(\varphi)}{E}\frac{c(\boldsymbol{r}, E, \varphi, \theta)}{G(E, \varphi, \theta)} \Delta E(E)\Delta\theta(E, \theta) \quad [\mathrm{m\, s^{-1}}] \tag{A8}$$

$$\underline{u_z}(\boldsymbol{r}) = \frac{2\pi\ 10^4}{16\, n(\boldsymbol{r})\, \tau}\sum_E \sum_\varphi \sum_\theta \frac{\cos(\theta)\sin(\theta)}{E}\frac{c(\boldsymbol{r}, E, \varphi, \theta)}{G(E, \varphi, \theta)} \Delta E(E)\Delta\theta(E, \theta) \quad [\mathrm{m\, s^{-1}}]. \tag{A9}$$

This paper has been typeset from a TEX/LATEX file prepared by the author.